

**Nonlocal rheological properties of granular flows near a jamming limit**Igor S. Aranson,<sup>1</sup> Lev S. Tsimring,<sup>2</sup> Florent Malloggi,<sup>3</sup> and Eric Clément<sup>3</sup><sup>1</sup>*Materials Science Division, Argonne National Laboratory, Argonne, Illinois 60439, USA*<sup>2</sup>*Institute for Nonlinear Science, University of California, 9500 Gilman Drive, San Diego, La Jolla, California 92093, USA*<sup>3</sup>*PMMH, UMR7636, CNRS-ESPCI-University, P6-P7, 10 Rue Vauquelin, 75005 Paris, France*

(Received 18 January 2008; revised manuscript received 19 June 2008; published 8 September 2008)

We study the rheology of sheared granular flows close to a jamming transition. We use the approach of partially fluidized theory (PFT) with a full set of equations extending the thin layer approximation derived previously for the description of the granular avalanches phenomenology. This theory provides a picture compatible with a local rheology at large shear rates [G. D. R. Midi, *Eur. Phys. J. E* **14**, 341 (2004)] and it works in the vicinity of the jamming transition, where a description in terms of a simple local rheology comes short. We investigate two situations displaying important deviations from local rheology. The first one is based on a set of numerical simulations of sheared soft two-dimensional circular grains. The next case describes previous experimental results obtained on avalanches of sandy material flowing down an incline. Both cases display, close to jamming, significant deviations from the now standard Pouliquen's flow rule [O. Pouliquen, *Phys. Fluids* **11**, 542 (1999); **11**, 1956 (1999)]. This discrepancy is the hallmark of a strongly nonlocal rheology and in both cases, we relate the empirical results and the outcomes of PFT. The numerical simulations show a characteristic constitutive structure for the fluid part of the stress involving the confining pressure and the material stiffness that appear in the form of an additional dimensionless parameter. This constitutive relation is then used to describe the case of sandy flows. We show a quantitative agreement as far as the effective flow rules are concerned. A fundamental feature is identified in PFT as the existence of a jammed layer developing in the vicinity of the flow arrest that corroborates the experimental findings. Finally, we study the case of solitary erosive granular avalanches and relate the outcome with the PFT analysis.

DOI: [10.1103/PhysRevE.78.031303](https://doi.org/10.1103/PhysRevE.78.031303)

PACS number(s): 45.70.Ht, 68.08.Bc

**I. INTRODUCTION**

Gravity-driven particulate flows are central to a variety of chemical technologies, the pharmaceutical, food, metallurgical and construction industries, as well as agriculture. These industries face serious challenges in the handling of granular materials, including their storage, transport, and processing. Furthermore, the transport properties of various natural particle-laden flows, such as dune migration, erosion-deposition processes, land slides, underwater gravity currents and coastal geomorphology, are staggered with many unresolved questions around the mechanics of the dense solid fraction motion. The dynamics of dense slowly sheared granular media [1,2] are strongly different from dilute rapid granular gases [3]. One of the distinct features of dense granular assemblies is the fluidization transition and the onset flow above a certain critical value of the shear stress. A comprehensive survey of granular flows in a variety of experimental settings and conditions performed by various groups around the world was conducted by a French research network Groupement De Recherche Milieux Divisés (MiDi) [1]. The salient feature of this work was to propose in the region of dense flow, not too close to jamming and of course, not in the domain of dilute flows where kinetic theory would prevail, a constitutive equation based on the existence of an effective friction coefficient. The constitutive relation solely depends on a single parameter, the inertia number  $I$  [1,4], which received a simple interpretation as the ratio of a microscopic reorganization time scale to a macroscopic time of shear (here, the elementary macroscopic volume is typically of one grain size). This approach was proven to be an essen-

tial step as it provides the correct phenomenology when tested against kinetic theories developed previously for the dilute flows. It was also successfully extended to take into account flows confined between rigid walls [5].

Nevertheless, a full picture of the rheology of granular flows is still lacking a conceptual clarity. Namely, the transition from a dense flow regime to a jammed phase remains a most debated issue [6–8]. In particular, systematic flow experiments with smooth glass beads on an inclined plane have established an empirical flow rule (also known as Pouliquen's flow rule) which has the remarkable property of rescaling all available data remaining fully compatible with a local friction coefficient picture. Nevertheless, one obtains a paradoxical situation where the associated effective friction coefficient involves a length scale describing how the granular flows jams (so-called stop height  $h_{\text{stop}}$ ) and this is quite far from the described flowing regime. Furthermore, recent experiments [9,10] and simulations [11] on the same systems have explicitly shown, in the close vicinity of jamming, deviations from the Pouliquen's flow rule, hence proving the nonlocality of the granular flow close to arrest. In addition, such a flow rule, relevant for model glass spheres, exhibits substantial deviations from experiment when other types of particles as rough sandy grains are used [1,12,13].

Since for dense, sheared granular assemblies, no full derivation of the constitutive relations is so far available, one needs to appeal to phenomenology. Several suggestions were made to justify the actual constitutive properties [14–17], but no consensus has been reached because the jamming of granular flows is still an area of active research. Some years ago, a continuum approach, the partial fluidization theory (PFT), was proposed in order to incorporate explicitly a de-

scription of a fluid-solid transition via a Landau-Ginzburg phenomenological theory of phase transitions. This approach allows for a nontrivial interpretation both of simulation data and of experiments [18,19]. It naturally incorporates the constitutive relations in terms of a solid stress tensor combined with a fluid stress tensor which is valid in a wide range of shear strain rates  $\dot{\gamma}$ . The momentum transport equations, valid on both sides of the jamming transition, allow us to describe a mixture of jammed and flowing phases. It nevertheless depends sensibly on the structure of the effective relations describing the phase transition and how the fluid and the solid stress components are mixed together.

This question is at the focus of the present paper. The PFT is extended to match quantitatively a set of numerical and experimental data. Several adjustments to the early formulation of the model parameters were made by comparisons with numerical and experimental results. For the sake of simplicity, a reduced set of equations have been derived in earlier works [18]; the momentum transport equations of the full PFT theory were approximated to obtain a more handy “thin layer limit.” The model also used a simplified constitutive approach to render the fluid phase (i.e., a viscouslike relation, independent of the confining pressure). Remarkably, even in this simplified form, all of the qualitative features found so far for erosion-deposition phenomena involving granular flows were reproduced [12,20,21], and some quite quantitatively. Note that recently this approach has also been used to describe real geophysical flows [22]. Important questions still remain such as how to connect the PFT more quantitatively to extended numerical results and to experimental data. Furthermore, one need to understand how different various flow conditions can be modeled as far as grain stiffness, shape or other granular features are concerned.

The structure of the paper is as follows. In Sec. II we discuss various models for sheared dense granular flows, including PFT, and their relation to the most recent experimental results. In Sec. III, we present the results of soft-particle numerical simulations. First we describe the simulation technique and then discuss the existence of an effective local rheology for an extensive set of simulations featuring a two-dimensional granular packing under shear. We also discuss the limitation of the previous approaches based on a single dimensionless parameter (inertia number  $I$ ). We give an interpretation of the results in the framework of the partial fluidization theory, and show how it can be extended such as to capture the existence of particle softness and the dependence of the liquid phase rheology with the confining pressure. This extended version of the PFT theory will be used to confront in the following sections, several experimental results.

In Sec. IV, flows of rough sandy grains down an incline will be considered. We will address specifically the question of flow rules and we will focus on the existence of a jammed layer at the bottom of the flow. The relation between the flow profiles derived from PFT and the experimental findings will also be addressed. Section V is dedicated to erosion-deposition waves. We will focus on the dynamics of a solitary erosion deposition wave and we will compared the PFT results to the outcome of experimental findings for rough sandy grains. Discussion and conclusion are in Sec. VI.

## II. BRIEF REVIEW OF THEORETICAL MODELS AND RELATION TO EXPERIMENTS

### A. Bagnold scaling

From heuristic dimensional arguments Bagnold proposed a simple local relation between the strain rate  $\dot{\gamma}$  and shear stress  $\sigma_{\text{shear}}$  [23],

$$\sigma_{\text{shear}} \sim d^2 \nu \dot{\gamma}^2. \quad (1)$$

This relation follows from the assumption that the only relevant time scale in a dense quasistatic granular flow is the deformation time scale  $T_\gamma \sim 1/\dot{\gamma}$ . This hypothesis was tested and improved in many subsequent presentations [4,14,24,25]. While the Bagnold relation (1) is likely satisfied in the bulk of a dilute granular flow, dynamic inhomogeneities in slow and dense granular flows result in substantial deviations from this simple scaling law. In addition, deviations from Bagnold scaling can stem from grain compressibility and cohesion [11,26].

### B. Pouliquen’s flow rule and local effective friction

A more general relation between shear stress and the strain rate has been recently proposed in a series of works [1,4,5,27]. In dense flows, the normal stress (pressure) is not directly related to the strain rate as in dilute regime, and must be included as an independent parameter. Pressure  $p$ , shear stress  $\sigma_{xy}$ , strain rate  $\dot{\gamma}$ , grain size  $d$ , and density  $\nu$  define two independent dimensionless parameters, the effective friction coefficient  $\mu_{\text{eff}}$  [28],

$$\mu_{\text{eff}} = \frac{\sigma_{xy}}{p} \quad (2)$$

and the dimensionless shear rate  $I$ ,

$$I = \frac{\dot{\gamma}d}{\sqrt{p/\nu}}. \quad (3)$$

The parameter  $I$  can be interpreted as the ratio of two different time scales, the deformation scale  $T_\gamma = 1/\dot{\gamma}$ , and the microscopic or confinement time scale  $T_p = d\sqrt{\nu/p}$ .

The volume fraction  $\Phi$  of granular flows (or, correspondingly, density  $\nu$ ) is another quantity controlling granular flows. One reasonable assumption is that the volume fraction is a function of the parameter  $I$ . In this situation one can find a unique local relation between the effective friction  $\mu_{\text{eff}}$  and the rescaled shear rate  $I$ . Experiments and numerical simulations indeed support the existence of a local relation between the effective friction  $\mu_{\text{eff}}$  and the scaled strain rate  $I$  for a variety of flows. In the most of the experiments the effective friction  $\mu_{\text{eff}}$  is a monotonously increasing function of  $I$  limited by the “static” friction value  $\mu_1$  for  $I \rightarrow 0$  and the dynamic friction value  $\mu_2$  for high values of  $I$ .

On the basis of extended experimental results, Pouliquen *et al.* [4,5,27] proposed the following relation between  $\mu_{\text{eff}}$  and  $I$  which fits most of the experimental data for glass beads:

$$\mu_{\text{eff}}(I) = \frac{\sigma_{xy}}{p} = \mu_1 + \frac{\mu_2 - \mu_1}{1 + I_0/I}. \quad (4)$$

Here  $I_0 \approx 0.279$  is a constant, and parameters  $\mu_1, \mu_2$  depend on the materials properties of grains.

### C. Flow rule

The flow rule relates the mean downhill velocity of a chute flow  $U_f = \int_0^h v_x(z) dz / h$  with its thickness  $h$  and with the chute angle  $\varphi$ . For the most studied experimental system, corresponding to monodisperse spherical glass beads flowing on rough substrates of glued beads, an empirical relation was obtained. It was shown that this relation allows us to collapse (within a precision of experiment) all experimental data onto a single curve for the dimensionless velocity  $U_f / \sqrt{gh}$  or Froude number  $\text{Fr}$  [1,2,5],

$$\text{Fr} = \frac{U_f}{\sqrt{gh}} \approx \beta^* \frac{h}{h_{\text{stop}}(\varphi)} \quad (5)$$

with constant  $\beta^* \approx 0.13$ ; here the characteristic height  $h_{\text{stop}}$  corresponds to the minimum thickness of the granular layer sustaining steady-state flow. Note that this relation is consistent with a local rheology  $\mu_{\text{eff}}(I)$ . It yields a ‘‘Bagnold velocity profile’’ characterized by a ratio  $r$  of the mean velocity  $U_f$  to the surface velocity  $V_s$ ,  $r = \frac{U_f}{V_s} = 3/5$ . More recent complementary measurements performed in the vicinity of the jamming limit  $h \rightarrow h_{\text{stop}}$  have extended this flow rule [9,10] to a more general form

$$\text{Fr} = \frac{U_f}{\sqrt{gh}} \approx \alpha^* \left( \frac{h}{h_{\text{stop}}(\varphi)} - 1 \right) \quad (6)$$

with  $\alpha^* \approx 0.22$ . Therefore, close to jamming, the rheology locality is now under question as a simple dependence of the effective friction  $\mu_{\text{eff}}$  against a single parameter  $I$  cannot work anymore. Moreover, experimental measurements of the velocity ratio yield  $r = U_f / V_s \rightarrow 1/2$ , i.e., a value corresponding to a linear shear flow.

Systems involving irregular grains such as rough sand often show substantial deviations from the standard Pouliquen’s flow rule [1,13] as well. In particular, the experiments revealed the existence of a static layer of thickness  $z_{\text{stat}}$  below the continuous flow and significant deviations of the ratio  $r = U_f / V_s \approx 3/5$  found for the flows of glass beads. We will discuss these issues below.

### D. Partial fluidization theory

A popular phenomenological approach to dense gravity-driven granular flows is based on the two-phase description of granular matter; one phase corresponding to rolling grains and the other phase corresponding to static ones. This approach, the so-called Bouchaud, Cates, Ravi Prakash, Edwards (BCRE) model, was suggested in Ref. [29] and was further elaborated on by many other research groups, see, e.g., Ref. [30].

However, in real granular flows there is no sharp distinction between a ‘‘rolling phase’’ and a ‘‘static phase.’’ The transition from a static to flowing regime is continuous. An attempt to develop a more general theory describing the non-stationary behavior of dense partially fluidized granular

flows was made in Refs. [18,19]. This theory is based on the intuitive idea that in dense granular flows a significant part of the stress is transmitted through quasistatic contacts between particles in addition to the ‘‘fluid’’ stresses transmitted through particle collisions and sliding friction. Thus, the stress tensor  $\sigma$  is represented as a sum of fluid and static components,

$$\sigma = \sigma^s + \sigma^f. \quad (7)$$

The key idea of PFT is that the separation of the stress tensor into static and fluid parts is controlled by the so-called order parameter,  $\rho$ . For the shear component of the stress, this separation is defined by a separation function  $q(\rho)$ ,

$$\sigma_{xy}^f = q(\rho) \sigma_{xy}, \quad \sigma_{xy}^s = [1 - q(\rho)] \sigma_{xy}. \quad (8)$$

Without loss of generality, the order parameter is scaled in such a way so that in granular solid  $\rho = 1$  and in a well-developed flow (granular liquid)  $\rho \rightarrow 0$ . On the ‘‘microscopic level’’ the order parameter can be defined as a fraction of the number of static (or persistent) contacts of the particles  $Z_s$  to the total number of the contacts  $Z$ ,  $\rho = \langle Z_s / Z \rangle$  within a mesoscopic volume which is large with respect to the particle size but small compared with the characteristic size of the flow. Defined in such a form the order parameter can be relatively easily extracted from the molecular dynamics simulations of soft particles [19]. The separation function  $q(\rho)$  must conform to two ‘‘boundary conditions’’  $q(\rho = 1) = 0$ ,  $q(\rho = 0) = 1$ . For the sake of simplicity, a linear dependence  $q = 1 - \rho$  was assumed in the first presentations [18]. More recently, we extracted this function from a two-dimensional soft particles molecular dynamics simulation, yielding a more specific dependence [31]

$$q(\rho) = (1 - \rho)^u \quad (9)$$

with  $u \approx 2.7$ . Note that the function  $q(\rho)$ , which fixes the mixing ratios between the static and the fluid parts of the stress might be material dependent. In the following, we will examine in more detail its influence on the jamming properties of the flow.

Due to a strong dissipation in dense granular flows the order parameter  $\rho$  is assumed to obey purely relaxational dynamics controlled by the Ginzburg-Landau-type equation for the generic first-order phase transition,

$$\tau \left( \frac{\partial \rho}{\partial t} + \mathbf{v} \cdot \nabla \rho \right) = l^2 \nabla^2 \rho - \frac{\partial F(\rho, \delta)}{\partial \rho}. \quad (10)$$

Here  $\tau$  is the characteristic time scale of the problem, and  $l$  is the order parameter ‘‘correlation length’’ which is assumed to be of the order of the grain size. These parameters can be scaled away by the renormalization of the length, time, and velocity

$$t_{\text{new}} = t / \tau, \quad \mathbf{r}_{\text{new}} = \mathbf{r} / l, \quad \mathbf{v}_{\text{new}} = \mathbf{v} \tau / l. \quad (11)$$

For the sake of brevity below we drop the subscript new.  $F(\rho, \delta)$  is a free energy density which is postulated to have two local minima at  $\rho = 1$  (solid phase) and  $\rho = 0$  (fluid phase) to account for the bistability near the solid-fluid transition. The relative stability of the two phases is controlled by the

parameter  $\delta$  which in turn is determined by the stress tensor. The simplest assumption consistent with the Mohr-Coulomb yield criterion is to take it as a function of “effective slope”  $\phi = \max|\sigma_{mn}/\sigma_{nn}|$ , where the maximum is sought over all possible orthogonal directions  $m$  and  $n$  (we consider here only two-dimensional formulation of the model). For planar two-dimensional shear flow we define the control parameter  $\delta = \phi = \sigma_{xy}/\sigma_{yy}$ . In the context of the flow on an inclined plane the parameter  $\delta$  is simply the slope of the plane,  $\delta = \tan \varphi$ , where  $\varphi$  is the inclination angle [19].

### III. SOFT PARTICLES UNDER SHEAR AND CONSTITUTIVE RELATIONS

#### A. Numerical techniques

To model the interaction of individual grains we use the so-called soft particles approach described in detail in Refs. [19,24]. The grains are assumed to be noncohesive, dry, inelastic disklike particles. Two grains interact via normal and shear forces whenever they overlap. For the normal impact we employ the spring-dashpot model [32]. This model accounts for repulsion and dissipation; the repulsive component is proportional to the degree of the overlap, and the velocity-dependent damping component simulates the dissipation. The model for shear force is based upon the technique developed by Cundall and Strack [33]. It incorporates tangential elasticity and Coulomb laws of friction. The elastic restoring force is proportional to the integrated tangential displacement during the contact and limited by the product of the friction coefficient and the instantaneous normal force. The grains possess two translational and one rotational degrees of freedom. The motion of a grain is obtained by integrating Newton’s equations with the forces and torques produced by the grains interactions with all of the neighboring grains and walls of the container.

The advantages and limitations of the employed contact force model were thoroughly studied by a number of authors [24,32]. In fact this is the simplest model accounting for both static and dynamic friction. All quantities are normalized by an appropriate combination of the average particle diameter  $d$ , mass  $m$ , and gravity  $g$  (while the simulation are performed for zero gravity, the gravity acceleration  $g$  is used only to construct formal time scale  $t_0 = \sqrt{d/g}$ ). Thus, distances,  $x, y$ , time,  $t$ , velocity,  $v$ , force,  $\tilde{F}$ , spring (elastic) constant  $k$ , and stress  $\sigma$ , are, respectively, measured in units of  $d, t_0, v_0 = \sqrt{dg}$ ,  $\tilde{F}_0 = mg$ ,  $k_0 = mg/d$ ,  $\sigma_0 = mg/d^2$ .

The equations of motion are integrated using the fifth-order predictor-corrector [34] with a constant time step. The spring constant  $k_n$  and damping coefficient  $\gamma_n$  were chosen to provide the desired value of the restitution coefficient  $e$  and guarantee an accurate resolution of an individual collision. Typically, we used a tangential friction coefficient between particles  $\mu_t = 0.5$ , we varied the dimensionless stiffness of the grains  $k_n$  in the range  $10^2 - 10^4$ , and we adjusted the viscous damping  $\gamma_n$  to obtain a fixed normal restitution coefficient  $e = 0.92$ . Simulations for smaller values of the restitution coefficient ( $e = 0.87$ ) produced qualitatively similar results. We also used the fixed ratio of the tangential and normal spring constants  $k_t/k_n = 1/3$ .

#### B. Simulation of a two-dimensional packing of soft grains under shear

The simulations were performed in two-dimensional geometry in the absence of gravity. The computational domain spans a  $50d \times 10d$  area, and is periodic in the horizontal direction  $x$ . The granulate is slightly polydisperse to avoid crystallization effects. We assume that the grain diameters are uniformly distributed around mean size  $d$  with 20% relative width. To provide a link between micromechanical quantities obtained through simulations and continuous fields, a coarse-graining procedure was applied [19]. Since all experiments described below deal with steady quantities, the procedure consists of two steps: space and then time averaging. The top and bottom “rough plates” were modeled by two straight chains of large grains (twice as large as an average particle diameter). The two plates were under fixed pressure  $p$ . The layer was chosen narrow enough, so the properties of the granular layer (shear rate, shear stress components, order parameter, etc.) were constant across the layer. Two opposite forces  $F_1 = -F_2$  were applied to the plates along the horizontal  $x$  axis to induce shear stress in the bulk. We started with large forces well above the fluidization threshold and slowly ramped them down in small increments until we reached the critical yield force at which the granular flow stopped. At every “stop” we let the system reach the stationary regime and measured all of the stress components, the strain rate, and the order parameter. Finally, we averaged the data over the whole layer and over the duration of each step. At any moment of time all contacts were classified as either “fluid” or “solid.” A contact was considered “solid” if it was in a stuck state ( $F_t < \mu_t F_n$ ) and its duration was longer than a characteristic time  $t_*$  which was slightly larger than collision time  $t_c$  (we used  $t^* = 1.1t_c$ ). The first requirement eliminates long-lasting sliding contacts, and the second requirement excludes short-term collisions pertinent to completely fluidized regimes. When either of the requirements is not fulfilled, the contact is assumed “fluid.” We define the order parameter as the ratio between space-time averaged numbers of “solid” contacts  $\overline{\langle Z_s \rangle}$  and all contacts  $\overline{\langle Z \rangle}$  within a sampling area [24],

$$\rho(y) = \overline{\langle Z_s \rangle} / \overline{\langle Z \rangle}. \quad (12)$$

We split the full stress tensor  $\sigma$  into the “solid” component,  $\sigma^s$ , and the “fluid” component,  $\sigma^f$ , in the same fashion as was done with contacts themselves.

The “fluid” part of the stress tensor is due to short-term collisional stresses and the Reynolds stresses, whereas the solid part accounts for persistent force chains. The Reynolds contribution to the stress is negligibly small in the vicinity of the phase transition, but comes into play when the granular aggregate is highly fluidized. In the system which is neither completely static nor completely fluidized we expect the coexistence (in time and space) of both phases. A particular grain may have both types of contacts at the same time thus contributing to both  $\sigma^f$  and  $\sigma^s$ .

#### C. Rheology and constitutive relations

Following the procedure outlined in the preceding section, we now report the rheology for a sheared two-dimensional

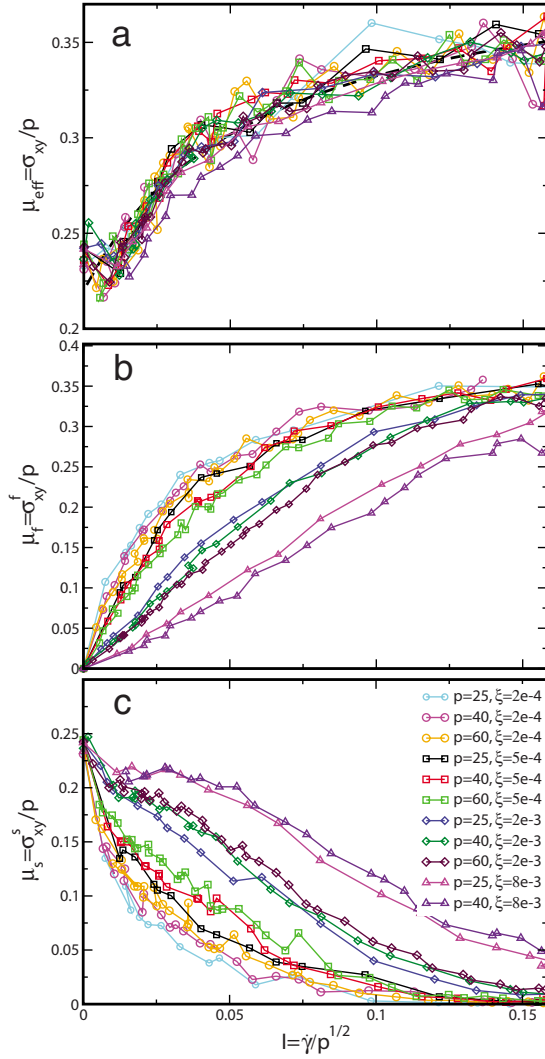


FIG. 1. (Color online) Effective friction  $\mu_{\text{eff}} = \sigma_{xy}/p$  (a), fluid friction  $\mu_f = \sigma_{xy}^f/p$  (b), and solid friction coefficient  $\mu_s = \sigma_{xy}^s/p$  (c) in planar shear cell experiment vs inertial parameter  $I = \dot{\gamma}/\sqrt{p}$  for various values of pressure  $p$  and values of the grain stiffness. Dashed line on the panel (a) depicts the friction law, Eq. (4), with parameters  $\mu_1 = 0.22$ ,  $\mu_2 = 0.4$ , and  $I_0 = 0.06$ .

granular packing. We performed multiple runs with  $N=500$  particles for several values of the pressure  $p$ , shear strain rate  $\dot{\gamma}$ , and inverse spring elasticity constant  $\xi$ . Figure 1(a) shows the full shear stress  $\sigma_{xy}$  normalized by the normal pressure  $p$  as a function of the dimensionless internal parameter  $I = \dot{\gamma}/\sqrt{p}$  (here and in the following unless explicitly stated, we set the grain size  $d=1$  and mass  $m=1$ ). We see that all data collapse rather well on a single curve (although there is a systematic drift of the data), and the elasticity of the grains appears to have little effect on the effective friction coefficient (friction slightly increases with the stiffness constant of grains). Our numerical data qualitatively agrees with the Pouliquen phenomenological law (4) with  $\mu_1 = 0.22$ ,  $\mu_2 = 0.4$ , and  $I_0 = 0.06$  [the original Pouliquen law, Eq. (4), gives  $I_0 \approx 0.279$ ; smaller value of  $I_0$  in our case is likely due to two-dimensional geometry of the simulation cell]. Now, in accord with the partial fluidization theory, we can proceed

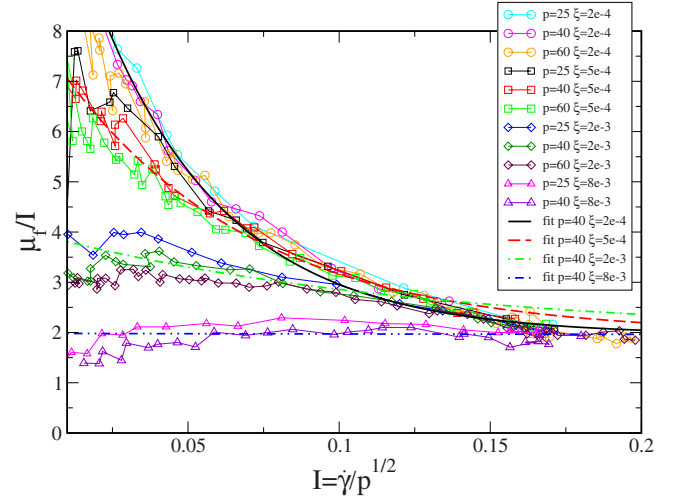


FIG. 2. (Color online) Scaled data for  $\mu_f/I = \sigma_{xy}^f/pI$  in planar shear cell experiment vs scaled strain rate (inertia parameter)  $I = \dot{\gamma}/\sqrt{p}$ .

further and separate the effective friction solid contribution from its fluid counterpart,

$$\mu_{\text{eff}} = \mu_s + \mu_f, \quad (13)$$

where  $\mu_s = \sigma_{xy}^s/p$  is the “solid” friction coefficient and  $\mu_f = \sigma_{xy}^f/p$  is the “fluid” friction. Both fluid and static components of the shear stress depend on the dimensionless internal parameter  $I = \frac{\dot{\gamma}}{\sqrt{p}}$  [see Figs. 1(b) and 1(c)]. Here we can see a significant spread of the data among runs with different particle’s elasticity parameter  $\xi = 1/k_n$ , and we observe a clear lack of data collapse with  $I$  in the limit of low shear rate or alternatively, softer particles.

For compressible grains, the softness, i.e., the inverse spring elasticity constant  $\xi = 1/k_n$ , brings a new time scale  $\tau_e = \xi^{1/2}$  and then one can build an additional dimensionless parameter  $S$  when it is compared with the confinement time scale  $T_p = 1/\sqrt{p}$  (see also Ref. [4] where a similar parameter was introduced),

$$S = \xi^{1/2} p^{1/2}. \quad (14)$$

Therefore, while the total effective friction is rather insensitive to the compressibility of grains, the relative contribution of the solid and fluid stress components depend significantly on the grain compressibility. This can be understood because softer grains can adjust their shape to maintain static contacts and therefore have greater proportion of shear stress carried by static contacts (somewhat similar conclusion was obtained in Ref. [11]).

In the following, we focus on the dynamics of the fluid component of the stress. The data suggest that for large  $I$  all of the curves appear to approach a certain asymptotic slope. It is more evident from Fig. 2 showing the ratio  $\mu_f/I$  vs  $I$ ,

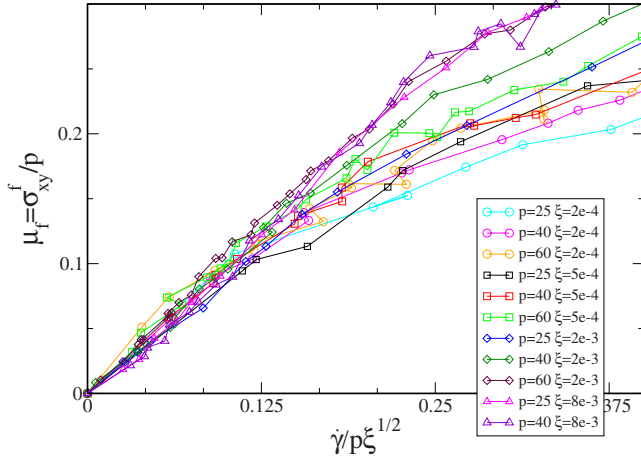


FIG. 3. (Color online) Scaled data of the fluid friction  $\sigma_{xy}^f/p$  in planar shear cell experiment against  $I/S = \dot{\gamma}/\sqrt{p}/S$ . Collapse of the data occurs for small strain rates.

$$\frac{\mu_f}{I} \rightarrow \mu_0 \approx 1.95. \quad (15)$$

Thus, our simulations suggest the following scaling of the fluid part of the stress tensor  $\sigma_{xy}^f$  vs shear strain rate  $\dot{\gamma}$  for sufficiently large strain rates  $\dot{\gamma}$ :

$$\sigma_{xy}^f = \mu_0 \sqrt{p} \dot{\gamma}. \quad (16)$$

While a similar expression was obtained earlier in Ref. [4], the result was interpreted as a manifestation of “generalized” Bagnold rheology with the effective viscosity diverging at the fluidization transition as  $\sim 1/(\Phi_c - \Phi)^2$  where  $\Phi_c$  is the closed packed solid fraction.

For small strain rate values we find that the data collapse occurs when  $\mu_f$  is plotted against the parameter  $I/S$  and is in fact controlled by the spring elasticity, see Fig. 3. For small strain rates the simulations suggest a different scaling,

$$\sigma_{xy}^f = \alpha \frac{\dot{\gamma}}{\xi^{1/2}}, \quad (17)$$

where  $\alpha \approx 1.05$  is another dimensionless constant. The fact that this constant is very close to 1 possibly implies that the elastic response is rather local (one or few grain sizes) and is related to a single grain deformability. Indeed, by the analogy with Eq. (3), constant  $\alpha > 1$  can be interpreted as an effective renormalization of the typical length [in Eq. (3) this length simply coincides with the grain size  $d$ ].

Correspondingly, for very small shear rates we obtain the following expression for the solid friction coefficient:

$$\mu_s = \mu_{\text{eff}} - \mu_f = \mu_{\text{eff}} - \alpha \frac{\dot{\gamma}}{p \xi^{1/2}} = \mu_{\text{eff}} - \alpha I/S, \quad (18)$$

where  $\mu_s \rightarrow \mu_{\text{eff}}$  for  $\dot{\gamma} \rightarrow 0$ .

To summarize, our simulations suggest two distinct scaling behaviors for small and large values of the strain rate. Therefore, the constitutive relation (4) is only approximate and valid for not too small values of the inertial parameter  $I$  determined by the condition  $I \gtrsim S$ . In general, the constitutive

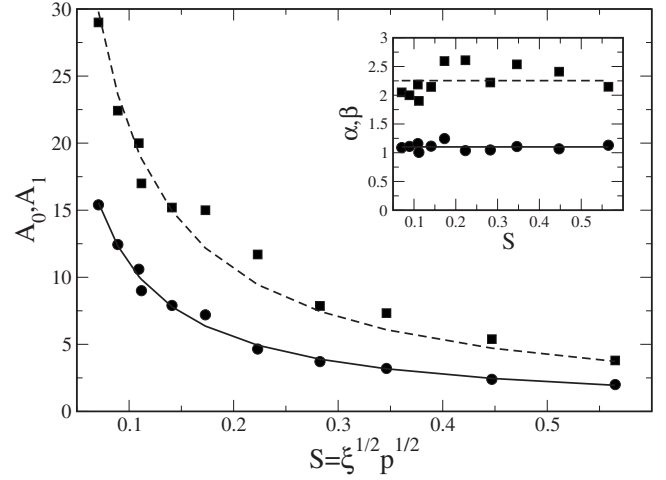


FIG. 4. Fitting of simulations data to Eq. (19). Each curve in Fig. 2 is fitted individually to the following expression:  $\sigma_{xy}^f/p = I[\mu_0 + (A_0 - \mu_0)\exp(-A_1 I)]$ ,  $\mu_0 = 1.95$ . The plot shows coefficients  $A_0$  (●) and coefficient  $A_1$  (■) vs  $S$ , solid line shows best fit  $A_0 = \alpha/S$  and dashed line  $A_1 = \beta/S$  correspondingly. Inset: Parameters  $\alpha = A_0 S$  (●) and  $\beta = A_1 S$  (■) vs  $S$ . Solid line shows  $\alpha = 1.05$  and dashed line  $\beta = 2.25$ .

relation should be the function of  $I$  and pressure  $p$ . We can describe the data in the whole range of  $p$  and  $\xi$  values by the following empiric law:

$$\frac{\mu_f}{I} = \mu_0 + \left( \frac{\alpha}{S} - \mu_0 \right) \exp(-\beta I/S). \quad (19)$$

The best fit for the simulation’s data shown in Figs. 1(b) and 2 yields the following values of the parameters:  $\mu_0 \approx 1.95$ ,  $\alpha = 1.05$ , and  $\beta = 2.25$ . Figure 4 shows the parameters of Eq. (19) in a wide range of the parameter  $S$ . As we see from Fig. 4, the parameters  $\alpha$  and  $\beta$  are almost constant over the whole range of  $S$  (more than a decade).

As it follows from Eq. (19), the transition between two scaling regimes occurs when the inertia parameter  $I$  becomes of the order of the compressibility parameter  $S$ . Thus, the corresponding value of the strain rate is  $\dot{\gamma}_c \approx \xi^{1/2} p$ . For very stiff grains ( $\xi \rightarrow 0$ ) the range of the second scaling given by Eq. (17) shrinks, and the rheology is described by Eq. (16) with a single parameter  $I$ , in agreement with Ref. [4]. Moreover, due to the exponential dependence of  $\mu_f$  on  $I/S$ , the last term in Eq. (19) is exponentially small for  $\xi \rightarrow 0$ , and, therefore, the single-parameter constitutive relation in the form  $\mu_f(I)$  is a rather accurate approximation in the majority of practical situations.

The parameter  $S$  is relevant (in numerical simulations or in real experiments) when the elastic moduli of the grains are comparable or much smaller than the confining pressure  $p$ . For gravity-driven avalanches it would mean that elastic moduli are of the order  $\nu g d$ , which is in practice quite unrealistic. However, for higher confining pressures acting on soft and highly compressible (e.g., polymeric) grains, this effect may become relevant and would justify the use of a modified rheology as described by relation (19).

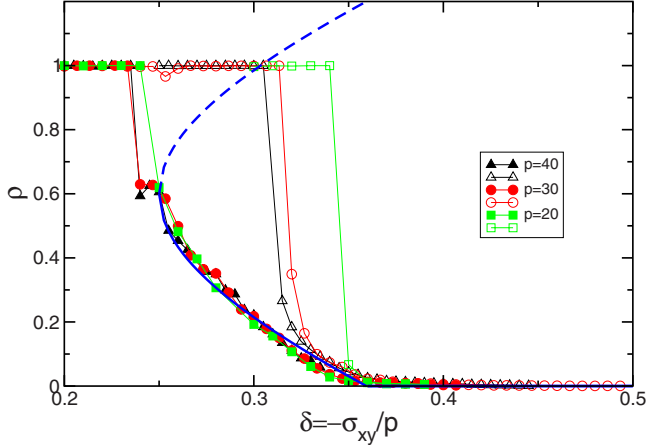


FIG. 5. (Color online) Bifurcation diagram for planar shear cell showing the order parameter  $\rho$  at steady-state regime vs control parameter  $\delta$  obtained from simulations for different values of applied pressure  $p$  (reproduced from [19]). Open symbols correspond to ramping up external driving force  $\bar{F}$ , and closed symbols corresponds to ramping down. Hysteretic behavior is evident. Thick lines show the fit to Eq. (20); solid lines indicate stable branch and dashed line unstable branch.

#### D. Calibration of the transition function

The zeroes of the transition function  $f$ , derived from the derivative of the “free energy density”  $(\rho-1)f=dF/d\rho$  [see Eq. (10)], can be obtained from the same simulations of shear flow as in the two-dimensional planar cell described in the preceding section, see Ref. [19] and Fig. 5. The overall behavior of the order parameter as a function of the control parameter  $\delta$ , i.e., ratio of shear stress to normal stress, can be summarized as follows: Ramping up the shear rate  $\delta$  results in an abrupt jump of the order parameter from the static solid value  $\rho=1$  to a small value  $\rho\approx 0.2$  (the onset of flow) at  $\delta\approx 0.3$  and further decrease of  $\rho$  towards zero with the increase of  $\delta$ . Ramping down the value of  $\delta$  from a well fluidized state results in a gradual increase in  $\rho$  and consequent jump from  $\rho=\rho_*\approx 0.6$  to  $\rho=1$  (flow arrest) at  $\delta\approx 0.25$  (hysteresis).

A good fit to the bifurcation diagram is given by the following simple expression:

$$f = \rho^2 - 2\rho\rho_* + \rho_*^2(1 - \zeta) \quad \text{for } \zeta < 1,$$

$$f = \rho^2 - \rho\rho_*(1 + \sqrt{\zeta}) \quad \text{for } \zeta > 1, \quad (20)$$

where  $\zeta = A(\delta^2 - \delta_0^2)$  with  $A=15$ ,  $\delta_0=0.25$ ,  $\rho_*=0.6$ .

The rationale for the expression (20) is the following: Equation (20) has the roots  $f(\rho_{1,2})=0$ ,  $\rho_{1,2}=\rho_*(1 \mp \sqrt{\zeta})$  for  $\zeta < 1$  and  $\rho_2=\rho_*(1+\sqrt{\zeta})$ ,  $\rho_1=0$  for  $\zeta > 1$ . Thus, one sees that one of the roots,  $\rho_2=\rho_*(1+\sqrt{\zeta})$ , remains identical for all  $\zeta$ . The other root,  $\rho_1=\rho_*(1-\sqrt{\zeta})$ , becomes identically zero for  $\zeta > 1$ . It prevents unphysical negative values of the order parameter for large  $\delta$  values. The parameters  $A$ ,  $\delta_0$  can be found on the basis of two-dimensional simulations or extracted from a comparison with experimental data.

#### E. Stability domain, $h_{\text{stop}}$ , $h_{\text{start}}$

The parameters  $\delta_0, A$  of the function  $f$  depend sensitively on material properties of grains. In order to extract these parameters from the chute flow experiment, we need to find the vertical profile of the order parameter  $\rho(z)$  for a steady-state flow on an inclined plane and calculate independently the value of  $h_{\text{stop}}$  for each value of the inclination angle  $\varphi$ . The flow velocity can be obtained from the constitutive relation for the fluid part of the stress.

The order parameter equation for steady-state shear flow is of the form [18,19]

$$\partial_z^2 \rho - (\rho - 1)f(\rho, \delta) = 0 \quad (21)$$

with the following boundary conditions: at the bottom  $z=0$  one imposes  $\rho(0)=1$  (rough bottom favor solid state), and on free surface  $z=h$  the most natural boundary condition is  $\partial_z \rho(h)=0$  (order parameter value is not fixed).

Parameters defining the transition function  $f$  can be then determined from matching the experimental values of  $h_{\text{stop}}$  and  $h_{\text{start}}$ , the value of thickness at which a static layer first becomes unstable at a given slope  $\varphi$  and corresponding parameter  $\delta$ . The value of  $h_{\text{start}}$  can be obtained from the linear stability analysis of the time-dependent equation (21). Substituting a solution of the form  $\rho=1+\epsilon \exp(\lambda t) \sin(\pi z/2h)$ ,  $\epsilon \rightarrow 0$ , we obtain for the growth rate of small perturbations  $\lambda = -f(1, \delta) - \pi^2/(4h^2)$ . The height  $h_{\text{start}}$  is obtained from the condition  $\lambda=0$ , which gives

$$h_{\text{start}} = \frac{\pi}{2\sqrt{-f(1, \delta)}}. \quad (22)$$

Using Eq. (20) one finds that  $h_{\text{start}} \rightarrow \infty$  for  $\zeta = A(\delta^2 - \delta_0^2) = (1/\rho_* - 1)^2$ . This condition defines the asymptotic static repose angle. For  $\delta \rightarrow \infty$  the value of  $h_{\text{start}}$  decreases as  $h_{\text{start}} \sim 1/\sqrt{\delta}$ .

In order to determine  $h_{\text{stop}}$  we need to find a nontrivial trajectory  $[\rho(z) \neq \text{const}]$  of Eq. (21) [18] satisfying the boundary conditions  $\rho(0)=1$ ,  $\partial_z \rho(z=h)=0$  and attaining minimal thickness of the layer  $h$ . This can be done by minimization of the length of trajectories of Eq. (21). Equation (21) can be integrated by multiplication on  $\partial_z \rho$  (see for detail [18]), yielding

$$(\partial_z \rho)^2 - 2F(\rho) = c_0, \quad (23)$$

where the “free energy density”  $F(\rho) = \int^\rho (\rho-1)f(\rho, \delta) d\rho$  and  $c_0$  is the constant of integration. Since  $\partial_z \rho=0$  at  $z=h$ , one can set  $c_0 = -2\int^{\bar{\rho}} (\rho-1)f(\rho, \delta) d\rho$ , where  $\bar{\rho}$  is the value of  $\rho$  at  $z=h$ . Thus,  $h_{\text{stop}}$  is given as

$$h_{\text{stop}} = \min \int_{\bar{\rho}}^1 \frac{d\rho}{\sqrt{2F(\rho) + c_0}}. \quad (24)$$

This integral can be evaluated numerically. Analytical estimates can be obtained for two cases,  $h_{\text{stop}} \rightarrow \infty$  and for  $\delta \rightarrow \infty$ . The value of  $h_{\text{stop}}$  diverges at  $\delta \rightarrow \delta_{\text{stop}}$ , i.e., the dynamic repose angle. The value of  $\delta_{\text{stop}}$  can be obtained analytically from the following consideration. The critical value of  $\delta = \delta_{\text{stop}}$  is defined by the condition that the length of non-trivial trajectory of Eq. (21) diverges, which corresponds to

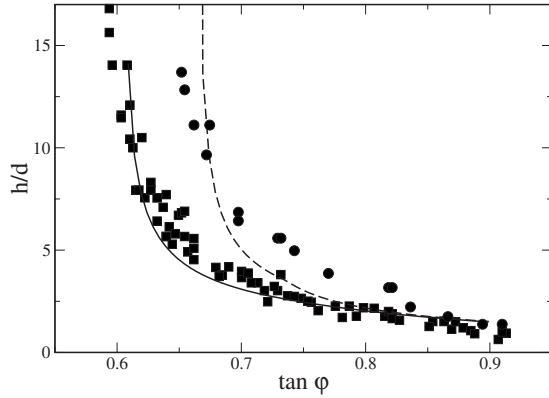


FIG. 6. Comparison of experimental data for sand on velvet with expressions for  $h_{\text{start}}$  and  $h_{\text{stop}}$ . Symbols are experimental points for  $h_{\text{stop}}$  (■) and  $h_{\text{start}}$  (●) [13,20], lines are fits according to Eq. (22) (dashed line) and Eq. (24) (solid line) with parameters  $\rho_* = 0.6$ ,  $A = 5.5$ ,  $\delta_0 = 0.6$ .

the existence of a separatrix connecting two fixed points,  $\rho = 1$  (solid) and  $\rho = \rho_1 = \rho_*(1 - \sqrt{\zeta})$  (liquid). Other trajectories of infinite length do not satisfy the boundary conditions. For the chosen form of the free energy  $F$  (fourth-order polynomial of  $\rho$ ) the existence of such a separatrix follows from the conditions that the fixed points of Eq. (21) are equidistant:  $1 - \rho_2 = \rho_2 - \rho_1$  [for more general form of  $F$  one should use the Maxwell rule  $\int_{\rho_2}^1 (1 - \rho) f d\rho = \int_{\rho_1}^{\rho_2} (1 - \rho) f d\rho$ ]. The condition of equidistant roots yields the following expression  $\delta_{\text{stop}}$  as function of parameters  $A, \rho_*$ :

$$A(\delta_{\text{stop}}^2 - \delta_0^2) = (1/\rho_* - 1)^2/9. \quad (25)$$

Then, the dependence of  $h_{\text{stop}}$  vs  $\delta$  for  $\delta \rightarrow \delta_{\text{stop}}$  can be obtained from integral (24) by expanding the denominator for  $\delta \rightarrow \delta_{\text{stop}}$  and  $\rho \rightarrow 1$ ,  $\tilde{\rho} \rightarrow \rho_1$ . The calculations results in the following behavior:  $h_{\text{stop}} \sim -\ln(\delta - \delta_{\text{stop}})$  for  $\delta \rightarrow \delta_{\text{stop}}$ .

In order to match  $h_{\text{stop}}$  and  $h_{\text{start}}$  curves, the outcome of PFT theory is compared with experimental data to find values of  $A, \delta_0$ . As one sees from Fig. 6 corresponding to the flow of sand on velvet [13,20], the best fit occurs for  $A = 5.5$  and  $\delta_0 = 0.6$ . However, there is some systematic deviation from experimental data, especially for  $h_{\text{start}}$  curve. It likely stems from the fact that we use a simplified function  $f$  [see Eq. (20)] which has been deduced from two-dimensional simulations of a relatively small system (500 grains only). Using a more complicated function  $f$  would certainly improve the agreement. However, it would also introduce additional adjustable parameters which we prefer to avoid for the sake of simplicity of analysis.

#### IV. FLOWS OF ROUGH SANDY GRAINS DOWN AN INCLINE

Experiments on smooth, nearly spherical beads have been widely used to extract the rheology of sheared granular assemblies in the inclined plane geometry [1]. As we mentioned earlier, the systems involving irregular grains (e.g., rough sand) often show substantial deviations from the stan-

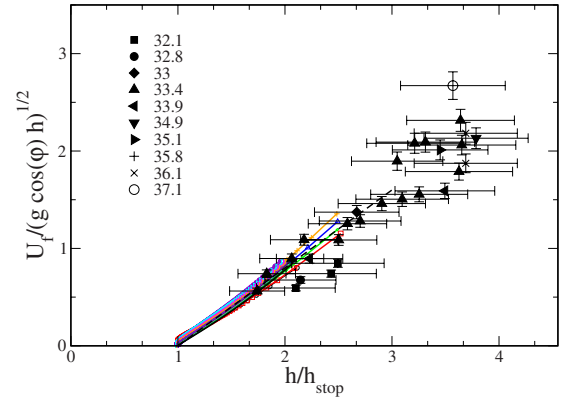


FIG. 7. (Color online) Effective flow rule  $U_f / \sqrt{g \cos \phi h}$  plotted against  $h/h_{\text{stop}}$ . The experimental results for different angles  $\phi$  are solid black symbols (corresponding angle  $\phi$  in degrees from  $\phi = 32.1^\circ$  to  $37^\circ$  is indicated in the legend to the plot). The results for PFT theory are solid lines. For better agreement with the experiment the value of parameter  $\mu_0$  is set to  $\mu_0 \approx 2$ , The dashed line is  $y = 0.8(x - 1)$ .

dard Pouliquen's flow rule [1,13]. The problem of the flow rule and the associated constitutive relation was studied earlier by Malloggi *et al.* [13] using Fontainebleau sand of a rather narrow size distribution [ $d = 300(\pm 60) \mu\text{m}$ ]. The shape of those grains was rough and faceted; very different from the regular spherical grains used by Pouliquen [2]. Now, we recall here briefly the most salient feature needed for a comparison with the PFT. The experimental system is similar to the one used by Daerr and Douady [20], and is represented by a flow of Fontainebleau sand over a velvet cloth. This system displays a rather wide bistability (hysteretic) domain between curves  $h_{\text{stop}}$  and  $h_{\text{start}}$ , see Fig. 6. To analyze the rheology of sand flows, an effective flow rule was obtained first, as in Ref. [1], by using the front velocity  $V_{\text{front}}$  of the avalanche spreading over the bare plane (see Fig. 7). Note that the identification of  $V_{\text{front}}$  with the mean (depth-averaged) flow velocity  $U_f$  is only valid when the flow goes down to the bottom of the plane. To identify the presence of a jammed (static) layer of sand below the continuous flow of grains, two independent experiments were then conducted.

Both experiments were conducted as close as possible to the regime of continuous steady-state flow. Correspondingly, the sand flux at the intake of the chute was determined by the opening of a reservoir filled with sand. Since the amount of granular material was limited, the duration of continuous flow in our experiments was between 50 and 500 seconds, depending on the flux values.

For the first experiment, a sooted blade was inserted in the flow inducing an erosion of the soot limited to the upper granular layers. After cessation of the flow, the blade was removed and photographed. A sharp transition between the eroded and the noneroded parts of the sooted blade was observed from the image processing of the soot gray levels. Our experiment shows that for the constant flux condition the transition height between eroded and noneroded soot parts was well defined. Consequently, the width of noneroded part was related to the width of the jammed layer.

For the second experiment, a sand deposit was prepared at a constant height close to  $h_{\text{stop}}(\phi)$ . Then, a trench spanning

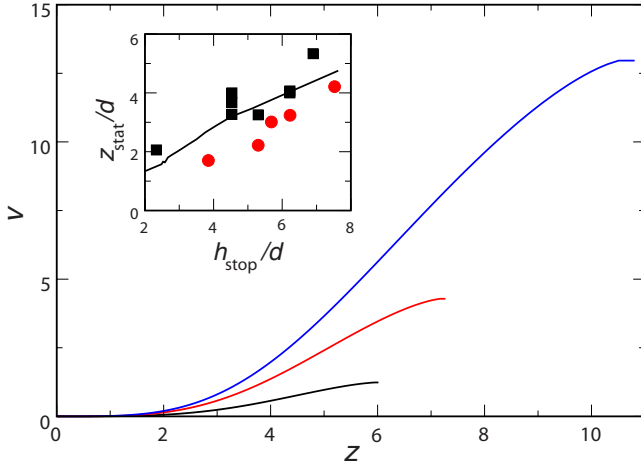


FIG. 8. (Color online) Representative vertical velocity profiles,  $V_x(z/d)$  for  $\delta=0.63$  ( $32.2^\circ$ ) at different driving fluxes. Inset: rescaled depth of the static layer  $z_{\text{stat}}/d$  vs  $h_{\text{stop}}/d$  (solid line). Symbols show that experimental data, squares show measurements using erosion methods and circles showing colored sand method (see text for explanations).

about 10 cm across and 2 cm along the slope at a downhill distance of about  $2/3$  of the plane length was dug down to the bottom of the deposit. Then, the trench was filled to the initial deposit height by packing layers by layer colored grains, with each layer corresponding to a different color. Once the deposit was reconstructed, the flow was initiated at some fixed flux value. After cessation of the flow, the deposit was excavated layer by layer and the remaining height of immobile grains was determined from the corresponding grain's color. Both experiments consistently confirmed the presence of a jammed layer (see inset of Fig. 8), at least for an experimental duration of continuous flow between 50–500 seconds.

Note that quasistatic or creeping layers were observed already in many other experiments, see, e.g., [5,7,35], but they likely stem from lateral boundary friction effects [5,36]. In the present case of sandy grain flow, the static layer comes from the interplay between rough bottom boundary and possibly, highly irregular shape of the grains. Indeed, in our experiments the avalanche plane had a width about 1200 times the grain size  $d$  and the resulting granular flows had a maximal height of about  $20d$ . The jammed layer is around 3 to 8 times the grains size maximum. Therefore, we can neglect the lateral boundary effects as a pertinent mechanism to induce a jammed layer and modify the flow characteristics [5,35,36]. Within experimental uncertainties, an empirical relation for the static layer was established as  $z_{\text{stat}}=Ad+Bh_{\text{stop}}$ , with the fitting constants  $A=-1.1(\pm 0.5)$  and  $B=0.7(\pm 0.1)$ . The ratio of the average velocity to the surface velocity,  $r=U_f/V_s$ , was measured as well. Note the values of  $r$  were found to differ consistently from the local rheology value:  $3/5$  and to increase with the rolling layer thickness  $R$  (see Fig. 9). The data points were found around an average value  $r=0.8(\pm 0.1)$ .

#### A. Calibration of the flow rule

In order to obtain the flow velocity we need to calculate the vertical profile of the order parameter  $\rho$  from Eq. (21). It

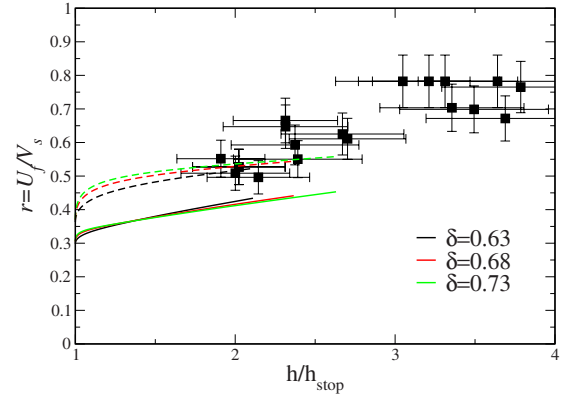


FIG. 9. (Color online) Values of velocity ratios  $r$  vs normalized flow depth  $h/h_{\text{stop}}$ . We have  $r=U_f/V_s$  where  $U_f$  is mean flow velocity,  $V_s$  is surface velocity, the symbols (■) display the experimental data for Fontainebleau sand, the solid lines are theoretical results for  $r$  obtained for  $u=2.7$  and three different values of  $\delta$ , and the dashed lines display  $r$  for the parameter values but for  $u=0.1$ .

can be easily done from the integral (23), which gives implicitly  $z(\rho)$ ,  $\tilde{\rho} < \rho < 1$ . Then the velocity is obtained from the constitutive relation

$$\sigma_{xz}^f = \mu_0 d \sqrt{p} \dot{\gamma} = q(\rho) \sigma_{xz}, \quad \mu_0 = \text{const}, \quad (26)$$

where function  $q(\rho)$  is calibrated from the relation,  $q(\rho) = (1-\rho)^u$ , see Eq. (9). In the following, we have used the value  $u=2.7$  obtained from the early numerical simulations [19]. However, we anticipate that in fact the value of  $u$  depends on material properties, such as tangential friction, grain shape, etc. We actually found that this parameter  $u$  controls the relative width of the jammed layer which increases with increasing of  $u$  and shrinks as  $u \rightarrow 0$ . Moreover, with the decrease in the value of the parameter  $u$ , the ratios of depth averaged to surface velocities  $r$  increases and approaches the  $2/3$  value corresponding to the ‘‘Bagnold’’ rheology, see Fig. 9.

In the chute flow geometry the shear stress is  $\sigma_{xz} = \sin \varphi (h-z)$  and the pressure is of the form  $p = \cos \varphi (h-z)$ . Thus, from the strain rate  $\dot{\gamma} = \partial_z v_x$  we obtain an equation for the downhill velocity in the rescaled variables

$$v_x(z) = \frac{\sin \varphi}{\mu_0 \sqrt{\cos \varphi}} \int_0^z q[\rho(z')] \sqrt{h-z'} dz'. \quad (27)$$

Then, the mean flow velocity  $U_f = h^{-1} \int_0^h v_x dz$  can be obtained by partial integration of Eq. (27),

$$U_f = \frac{1}{h} \int_0^h v_x(z) dz = \frac{\sin \varphi}{\mu_0 \sqrt{\cos \varphi}} \int_0^h q(\rho) (h-z')^{3/2} dz'. \quad (28)$$

Then, for each value of  $\delta$ , we determined the value of  $h_{\text{stop}}$  and mean flow velocity  $U_f$  in the range of all possible flow thicknesses,  $h_{\text{stop}} < h < h_{\text{max}}$ , where  $h_{\text{max}}$  is the maximal depth above which the steady-state flow for a given value of the angle  $\varphi$  either ceases to exist or become unstable.

Here we must comment that the accessible range of thicknesses  $h/h_{\text{stop}}$  is somewhat smaller than that in the experiment since we consider steady-state flow only. There are several factors limiting the range of existence for the steady-state flow. As we showed early in Ref. [18], for each value of the slope angle  $\varphi$  the stationary flow regime persists up to some critical thickness. A further increase in flow width  $h$  leads to gradual accumulation of the granular matter down the flow direction and, consequently, readjustment of the slope angle. Also, for very high flow rates the flow may become unstable with the transition to accelerating flow [2]. Alternatively, with the decrease in the flow width  $h$ , the flow may become unstable with respect to long-surface wave instability (so-called Kapiza waves [37]). As we have shown in Ref. [6], the Kapiza waves phenomenon is also captured in the framework of partial fluidization theory. Note also that the Kapiza waves are also observed for sandy grain flows in this range of Froude numbers [37].

Overall, 15 curves derived from the PFT theory are displayed in Fig. 7. They correspond to a broad range of slopes from  $\delta=0.61$  (angle  $\varphi=31.4^\circ$ , close to  $\delta_{\text{stop}}$  in Fig. 6) up to  $\delta=0.93$  ( $\varphi=42^\circ$ ). As one sees, all curves, theoretical and experimental, show the same tendency to cluster near a single line but differently from the Pouliquen flow rule: The lines do not have intercepts at the origin. We may also note that within the data scatter, a line going through  $(h/h_{\text{stop}}=1, \text{Fr}=0)$  would be a first order fair representation of this raw flow rule. Note that this is qualitatively similar to the data of Deboeuf *et al.* [10] in the vicinity of jamming. Unfortunately, the presence of various instabilities discussed above prevents us from going simply to much higher values of  $h/h_{\text{stop}}$ .

Here, we chose to display the Froude number  $\text{Fr} = U_f / \sqrt{gh \cos(\varphi)}$  with the  $g \cos \varphi$  component that represents the actual confining part of the pressure in an avalanche experiment. Nevertheless, this choice made for the sake of consistency with a theoretical description using an effective rheology, has no practical influence on the results and on the effective flow rule, because of the remaining data scatter. Therefore, this choice of parameters provides a quantitative agreement, not only for the stability diagram but also for the effective flow rule.

Note that we also explored the flow rule for a generalized constitutive relation in the generalized form (19) found for soft spheres. It produced only a slight improvement, but qualitatively the results remain the same. Thus, we conclude that the part of the constitutive relation associated with the grain compressibility is not manifested in the flow rule at typical parameter values.

## B. Velocity profile and the onset of flow

Now we focus on the flow profiles near the onset. Figure 8 shows the vertical velocity profiles obtained from Eq. (27) for different values of  $h$ . As one sees, for this choice of parameter, all velocity profiles display a quasistatic layer  $z_{\text{stat}}$  where the velocity is almost zero.

In the flowing layer the velocity changes almost linearly, except for a small boundary layer (due to no-flux boundary condition) at the free surface. The velocity profiles are simi-

lar to those obtained in simulations for flows over a rough bottom, see [1]. Therefore, the quasistatic layer is a new intrinsic feature of partially fluidized flows at the onset of flow (jamming). It corresponds to a region where the velocity is significantly smaller than the mean (or the surface) velocity. This also could be called a creeping region. It is rather challenging to measure the velocity profiles in the static layer. One can only test if the displacement of the grains at a given location in the bulk are noticeable over the duration of the experiment (in practice limited by the available mass of grains). In this work, we define the location of the static layer by the condition  $v(z=z_{\text{stat}})=0.1v(z=h)$  (other threshold conditions give similar results). Moreover, our studies show that the static layer thickness  $z_{\text{stat}}$  does not practically depend on the total flow thickness (or total grain flux). It allows to parametrize the dependence of  $z_{\text{stat}}$  on the value of  $h_{\text{stop}}$  only, as it is shown in the inset of Fig. 8.

As it follows from Fig. 8, the depth of the static layer shrinks with the decrease of  $h_{\text{stop}}$ , i.e., with the increase of the slope angle  $\varphi$ . For comparison, we show the experimental data for  $z_{\text{stat}}$  normalized by the grain size for the two different methods described earlier. It turns out that the numerical data goes right in between the experimental points that can be viewed as higher and lower bounds for the determination of the static layer. To obtain insight into the flow profiles and the relationship between theory and experiment, we compared different flow velocity ratios. Note that for the Bagnold flow with a velocity going down to zero at the bottom of the chute one obtains a ratio of the mean flow (equal to  $U_f$ ) to the surface flow  $V_s$  with a value  $r=0.6$ . Our analysis shows that the apparent value of  $r=U_f/V_s$  is of the order of 0.3 for  $h \rightarrow h_{\text{stop}}$  and gradually increases approaching the value 0.45 with the increase in flow thickness  $h$ . Thus, the apparent ratio  $r$  is smaller than that of the Bagnold or linear velocity profile, which is obviously due to the presence of a static layer. For comparison, Fig. 9 depicts ratios  $r=U_f/V_s$  for both theory and experiment. The experimental and theoretical domains for the corresponding values of  $h/h_{\text{stop}}$  only weakly overlap. Nevertheless, in both cases, we evidence an increase of  $r$  at larger flowing heights. However, it seems that for this choice of theoretical parameters, the experimental values ( $0.5 < r < 0.55$ ) are slightly higher in the overlapping domain than the theoretical one,  $0.4 < r < 0.45$ . Furthermore, the theoretical analysis also indicates that the value of  $r$  depends on the value of the exponent  $u$  in Eq. (9):  $r$  increases with the decrease of  $u$ , as it is illustrated in Fig. 9. The corresponding flow rule is also closer to what was found by [10] for an assembly of rough glass spheres, where a crossover between a Pouliquen-like flow rule and a line intercepting at zero for  $h/h_{\text{stop}}=1$  was observed.

For larger values  $h/h_{\text{stop}} \approx 4$  the parameter  $r$  increases and approaches the 0.8 which can be interpreted as a formation of a plug flow [ $v_z(z) \approx \text{const}$ ]. However, on the qualitative level the formation of a plug flow profile could be treated as a strong velocity gradient in the jammed region which would act almost as an effective finite velocity slip at the scale of one grain. It would be interesting to see if the PFT model pushed in the limit of thick flows (gravity surface waves included) would be able to describe this feature.

Our study shows that after a thorough calibration against experiments, we are in a position to provide a clear-cut vi-

sion of capacities and limitations of the PFT. It becomes clear that a crucial issue is the choice of a mixing function between the solid and the liquid phases (described here by the exponent  $u$ ). Adjusting this parameter yields a flow that looks more like a plug flow since the capacity to mix solid and liquid can be rendered very sharp. However, this also limits the calibration of the PFT since we do not have at the moment a theory to justify a proper choice of this critical parameter. Therefore, we leave this nontrivial problem to future studies.

## V. EROSION DEPOSITION WAVES

### A. Experimental solitary waves

Propagating avalanches on an erodible layer of grains were studied experimentally on glass bead layers [8,20] as well as on sandy layers [8,12,13,21]. A particularly interesting family of such avalanches are solitary waves [12,13,21]. In order to produce such stable solitary erosion-deposition wave, the following experimental technique is used. After the deposition of a layer of grains at  $h=h_{\text{stop}}$  a mass of grains is scraped by a bulldozer technique (see [12] for details). Beyond a minimal mass of grains,  $m_c$ , set into motion, one obtains a solitary (or autonomous) avalanche. As the layer thickness left behind the wave is the same as in the front, the mean moving mass is thus conserved [see Fig. 10(a)]. These solitary waves have an asymmetric “shark-teeth” shape. The velocity of this solitary wave  $v_a$ , which is on the order of  $\sqrt{gd} \cong 5-10$  cm/s, quickly saturates to a certain asymptotic value. The asymptotic velocity is an increasing function of the mass of grains set into motion. For a given angle, there is a family of solitary avalanching solutions. Nevertheless, if a mass set into motion is too large, the avalanche will split into smaller pieces in order to maintain avalanching masses compatible with an upper critical value depending on the inclination angle. Analysis of the surface velocity and the corresponding avalanche profile exhibit three distinct regions [see Fig. 10(a)]: (i) the front, where inertia is important,  $1100 < x/d < 1200$ , (ii) the central body,  $500 < x/d < 1100$ , where inertia is not relevant and for which the height and the velocity are related, and, finally (iii) a tail region,  $x/d < 500$ , where  $h \approx h_{\text{stop}}$  is reached and only about one layer of beads is still rolling on the surface. These are general and robust features of such an erosion-deposition wave. This solitary wave phenomenology is an important situation since it creates an opportunity to gain insight into the dynamics of erosion-deposition processes very close to the jamming onset; an issue which is still unclear from its basic physical stand point. Moreover, as we will see below, it allows the possibility of a unique direct comparative study with the partial fluidization theory.

### B. Theoretical analysis using PFT

The model of avalanches proposed by Savage and Hutter [38] is based on a depth-averaged description (so-called Saint-Venant-type approach) with an effective basal friction coefficient. The constant value of the friction coefficient cannot assure a stability of steady flow. In more recent versions

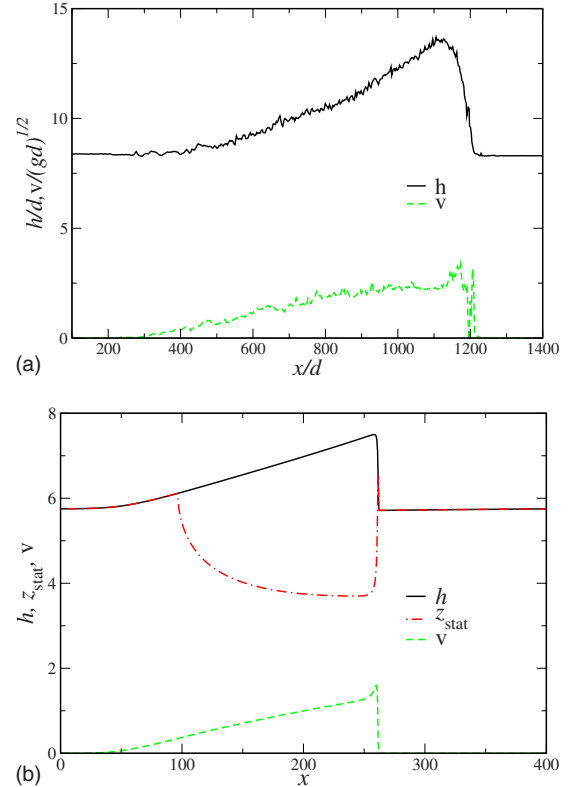


FIG. 10. (Color online) Solitary avalanche profiles. (a) Experimental profiles of avalanche height  $h$  and surface velocity  $v$  on Fontainebleau sand at an angle  $\varphi=32^\circ$  and for a trapped mass onset  $m_c=8900(\pm 200)d^2$ . The avalanche velocity is  $v_a=1.9(\pm 0.1)(gd)^{1/2}$ . (b) Numerical profiles  $h(x)$ ,  $v(x)$  and static layer depth  $z_{\text{stat}}$  from the PFT theory for  $\delta_0=0.633$  (or  $\varphi=32.3^\circ$ ),  $h_{\text{stop}}=5.8$ .

of this model, Pouliquen and Forterre [39] have refined the scheme by introducing a rate-dependent flow rheology that describes more successfully this phenomenon. However, this approach is unable to handle properly the phenomenology in the metastable region as well as erosion-deposition mechanisms occurring in the bulk of an avalanche. Furthermore, it cannot provide detailed information on the vertical flow profiles.

The analysis of avalanches in earlier work [21] was implemented for a simplified rheology assuming pressure-independent viscosity and very thin granular layers when the formation of a static layer was unimportant. Already, at a qualitative level, the essential phenomenology of pattern formation was recovered such as avalanche velocity selection, shape, transversal instability. Now, we want to pursue the refinement of the PFT by incorporating a more realistic rheology and to obtain information of the dynamics of the jammed layer. In Ref. [21] the avalanches were analyzed when the vertical structure of the order parameter was fixed and the static layer was ignored, allowing for reduction of Eq. (10) to a much simpler model. However, this approximation breaks down in thicker layers. In order to describe avalanches in deeper layers, one needs to solve directly Eq. (10) in two-dimensional geometry  $(x,z)$  with a free surface boundary condition. Thus, the following equation was solved numerically:

$$D\rho/Dt = (\partial_z^2 + \partial_x^2)\rho - (\rho - 1)f(\rho, \delta), \quad (29)$$

where function  $f$  is given by condition (20),  $D/Dt$  is a material derivative. The evolution of layer thickness  $h$  was obtained from the mass conservation condition

$$\partial_t h = -\partial_x J \quad (30)$$

with the flux  $J = \int_0^h v(z) dz = hU_f$ , see Eq. (28). We take into account that local angle changes also due to the change in layer thickness  $h$ , i.e.,  $\delta = \delta_0 - \partial_x h$ ,  $\delta_0 = \tan \varphi_0 = \text{const}$ . Thus, it gives rise to the equation

$$\partial_t h = -\frac{\sin \varphi_0}{\mu_0 \sqrt{\cos \varphi_0}} \partial_x \left( (1 - \partial_x h / \delta_0) \int_0^h q(\rho)(h-z)^{3/2} dz \right). \quad (31)$$

We solved Eqs. (29) and (30) using the following method. Equation (29) was solved on rectangular domain  $N_x \times N_z$ , periodic in the  $x$  direction, with the boundary conditions  $\rho = 1$  for  $z=0$ ,  $\partial_z \rho = 0$  for  $z=h$ . Equidistant mesh was used in the  $x$  direction. In the  $z$  direction the mesh size was scaled by  $h$ ,  $dz = h(x)/N_z$ . Correspondingly, the height  $h$  was obtained from Eq. (31). We used  $N_x = 800$ ,  $N_z = 50$ , and length in the  $x$  direction  $L = 400$ . As an initial condition we choose localized bump. After some transient the bump turns into localized avalanche traveling with a constant speed. In Fig. 10, we show the stationary profile obtained at  $\varphi \approx 32^\circ$ . The shape of the avalanche and the velocity profile are qualitatively similar to the experimental observations. However, the numerical value for the maximum height is lower than in the experiment. From the numerical results, we were also able to obtain the depth of the static layer beneath the moving avalanche,  $z_{\text{stat}}$ . As one sees from Fig. 10, only a small fraction of the sand is fluidized ( $z_{\text{stat}} < z < h$ ) in the course of avalanche propagation; the rest of the material is in a static state. Moreover, the surface velocity  $v(x)$  has a characteristic peak similar to that observed in the experiment [12]. However, for the present set of model parameters, the width of the experimental avalanche is about 2–3 times larger than that of the theoretical outcome, see Fig. 11. Note also that both experimentally [13] or numerically [21] a small increase of the width occurs with the trapped mass (less than 20%). Experimentally, the data were taken at the onset of the critical mass for solitary wave propagation. This result suggests that there is a need for a systematic exploration of the simulation parameters in order to see if there is the possibility for a given class of material to match quantitatively (i) flow rule, (ii) velocity ratios, and (iii) solitary avalanche features. This is up to now the most stringent series of tests for any theoretical description of erosion-deposition processes in granular matter. In the context of PFT, we leave this systematic exploration for a future report.

In addition, as one can see in Fig. 11, the tail of experimental solitary wave is significantly larger than that of the PFT solution. In experiment, a significant fraction of the solitary-wave back tail corresponds to a very thin layer of grains still flowing at  $h = h_{\text{stop}}$ . It is likely that this fraction of the tail is moving because of internal vibrations of grains (sound modes) present in the rear of the avalanche in spite of

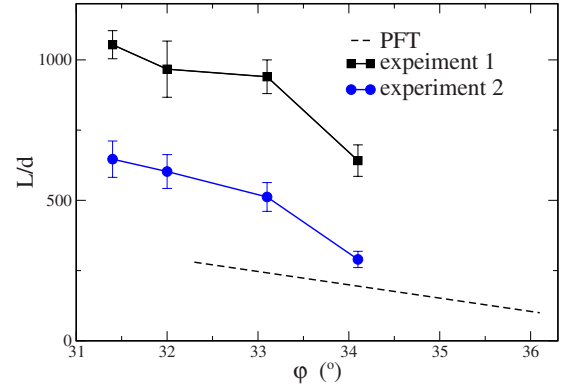


FIG. 11. (Color online) Width of the solitary wave  $L$  vs angle  $\varphi$  (in degrees) in experiment and theory. Experimental curve 1 depicts entire length of the avalanche, and experimental curve 2 shows the original length minus a tail part where  $h \approx h_{\text{stop}}$  within 1 grain size (see discussion below).

the fact that thickness of granular layer  $h$  reaches  $h_{\text{stop}}$ . To illustrate this point, we show in Fig. 11 the original wave-length minus a part corresponding to a significant surface flow at  $h = h_{\text{stop}}$  (within one grain size), which roughly comprises one-half of the total length. This effect is not captured by the PFT as it is likely due to a coupling between the flow and the internal vibrational degrees of freedom. Indeed, since at  $h = h_{\text{stop}}$  the granular packing is close to arrest, it is apparently in a very fragile state. Thus, the flow conditions are likely to be modified by small internal or external vibrations. Note also that a similar effect was indirectly observed in an earlier paper, Ref. [18], when comparing numerical simulations with PFT results [see Fig. 2(a) in Ref. [18]]. It turns out that in numerical simulations for thin layers, the velocity at the liquid-solid transition is almost continuous. On the contrary, the PFT exhibits a discontinuous transition.

## VI. CONCLUSIONS

In this paper we focused on the rheological properties of dense sheared granular flows. On the basis of two-dimensional molecular dynamics simulations, we were able to propose constitutive relations for stresses in partially fluidized granular flows. We found that the “universal” single-parametric constitutive relation proposed in Refs. [2,5,27] is in fact valid only for not too small values of the normalized strain rates. For smaller strain rates the stiffness of grains comes into play and rather different scalings between shear stress, strain rate, and pressure ensues. The scaling is characterized by dimensionless parameter  $S$  relevant when the elastic moduli of the grains are comparable or much smaller than the confining pressure  $p$ . While in a recent work by da Cruz *et al.* [4], similar numerical evidence was obtained, in our work we were able to incorporate the effects of finite grain elasticity in the generalized constitutive relation (19). Our results emphasize the importance of grain compressibility when the local contact forces induce deformations that are likely to change the contact configuration faster than a gravity driven grains rearrangement. However, for the laboratory-scale gravity-driven flows down an incline this

behavior can be observed only for very soft and compressible particles (e.g., polymeric grains) with the elastic moduli are of the order  $\nu g d$ . For gravity-driven avalanches of glass beads or sand this assumption is rather unrealistic, so the additional scaling regime for very small shear rates could be very hard to observe.

An experimental verification of our findings through measured stress-strain relationships for particles with different elasticity but in otherwise identical experimental conditions is highly desirable. Another important issue is the effect of dimensionality and particle roughness. While we believe that our two-dimensional simulations are representative and correspond to the actual phenomena, at least on a qualitative level, further three-dimensional checks are needed. We demonstrated that the flow rule for granular flows in a thin chute with rough bottom [1] can be deduced from the partial fluidization theory. According to our theory, the flow rule appears to be satisfied only approximately, with small but systematic deviations from a universal master curve. However, since our theoretical model is also based on approximate expressions for the free energy and for the constitutive relations, the existence of an exact flow rule where all curves would collapse remains an open question. Another interesting question in this context is what needs to be changed in the partial fluidization theory in order to obtain different flow rules, especially in the vicinity of jamming. In the framework of PFT, it is feasible that for both the free energy and the order parameter “mixing” function  $q(\rho)$  must be changed to match a given experimental system. Unlike our previous studies, we were able to extend our calculations beyond the regime of thin chute flow. We adjusted the outcome of the PFT in order to match avalanche experiments performed

with sand on a rough incline. We obtain a quantitative agreement with the effective flow rule, different from the Pouliquen’s flow rule, where the corresponding Froude number vanishes as the stopping height  $h_{\text{stop}}$  is approached. Furthermore, for this set of parameters, the existence of a creeping layer spontaneously forming beneath the well-fluidized part of the avalanche is observed, in agreement with the experimental findings. In addition, in the framework of PFT we identified an important feature associated with the “mixing” function  $q(\rho)$  that is essential to render the existence of a jammed layer and, thus, allowing for more close comparison with a given class of granular material.

Finally, we used a complete set of equations for partial fluidization model in order to study the shape of the solitary avalanches flowing down a rough inclined plane. For most of the measured features, the results are in a qualitative agreement with the experimental measurements on sand. However, in the present form, the PFT underestimates the width of the experimental avalanche by a factor of 3. Excitation of internal vibrational degrees of freedom (sound modes) in the tail of sandy avalanche is proposed as one of the possible reasons for this discrepancy. This effect is not currently incorporated in the PFT and is left for the future studies.

#### ACKNOWLEDGMENTS

We thank D. Volfson for help with numerical simulations and useful discussions. I.A. and L.T. were supported by US DOE, Office of Science, Contracts No. DE-AC02-06CH11357 and No. DE-FG02-04ER46135. E.C. and F.M. were supported by the ANR project PIGE “Physique des Instabilités Gravitaires et Erosives.”

- 
- [1] G. D. R. Midi, *Eur. Phys. J. E* **14**, 341 (2004).
  - [2] O. Pouliquen, *Phys. Fluids* **11**, 542 (1999); **11**, 1956 (1999).
  - [3] N. V. Brilliantov and Th. Pöschel, *Kinetic Theory of Granular Gases* (Oxford University Press, Oxford, 2004).
  - [4] F. da Cruz, S. Emam, M. Prochnow, J.-N. Roux, and F. Chevoir, *Phys. Rev. E* **72**, 021309 (2005).
  - [5] P. Jop, Y. Forterre, and O. Pouliquen, *Nature (London)* **441**, 727 (2006).
  - [6] I. S. Aranson and L. S. Tsimring, *Rev. Mod. Phys.* **78**, 641 (2006).
  - [7] R. Delannay, M. Louge, P. Richard, N. Taberlet, and A. Valance, *Nat. Mater.* **6**, 99 (2007).
  - [8] T. Börzsönyi and R. E. Ecke, *Phys. Rev. E* **76**, 031301 (2007).
  - [9] G. Felix and N. Thomas, *Earth Planet. Sci. Lett.* **221**, 197 (2004).
  - [10] S. Deboeuf, E. Lajeunesse, O. Dauchot, and B. Andreotti, *Phys. Rev. Lett.* **97**, 158303 (2006).
  - [11] L. E. Silbert, G. S. Grest, R. Brewster, and A. J. Levine, *Phys. Rev. Lett.* **99**, 068002 (2007).
  - [12] F. Malloggi, J. Lanuza, B. Andreotti, and E. Clément, in *Powders and Grains*, edited by R. Garcia-Rojo, H. J. Herrmann, and S. McNamara (Balkema, Rotterdam, 2005); *Europhys. Lett.* **75**, 825 (2006).
  - [13] F. Malloggi, A. Fourrière, B. Andreotti, P. Claudin, and E. Clément (unpublished).
  - [14] D. Ertas and T. C. Halsey, *Europhys. Lett.* **60**, 931 (2002).
  - [15] A. Lemaitre, *Phys. Rev. Lett.* **89**, 064303 (2002); **89**, 195503 (2002).
  - [16] K. Kamrin and M. Z. Bazant, *Phys. Rev. E* **75**, 041301 (2007).
  - [17] J. T. Jenkins, *Phys. Fluids* **18**, 103307 (2006).
  - [18] I. S. Aranson and L. S. Tsimring, *Phys. Rev. E* **64**, 020301(R) (2001); **65**, 061303 (2002).
  - [19] D. Volfson, L. S. Tsimring, and I. S. Aranson, *Phys. Rev. E* **68**, 021301 (2003).
  - [20] A. Daerr and S. Douady, *Nature (London)* **399**, 241 (1999).
  - [21] I. S. Aranson, F. Malloggi, and E. Clément, *Phys. Rev. E* **73**, 050302(R) (2006).
  - [22] A. Mangeney, L. Tsimring, D. Volfson, I. S. Aranson, and F. Bouchut, *Geophys. Res. Lett.* **34**, L22401 (2007).
  - [23] R. A. Bagnold, *Proc. R. Soc. London, Ser. A* **225**, 49 (1954).
  - [24] L. E. Silbert, D. Ertas, G. S. Grest, T. C. Halsey, D. Levine, and S. J. Plimpton, *Phys. Rev. E* **64**, 051302 (2001).
  - [25] L. Bocquet, W. Losert, D. Schalk, T. C. Lubensky, and J. P. Gollub, *Phys. Rev. E* **65**, 011307 (2001).
  - [26] R. Brewster, G. S. Grest, J. W. Landry, and A. J. Levine, *Phys. Rev. E* **72**, 061301 (2005).

- [27] O. Pouliquen and Y. Forterre, *J. Fluid Mech.* **453**, 133 (2002).
- [28] Somewhat similar formulation of the rheology for dense granular flows was suggested earlier by J. D. Goddard, *Acta Mech.* **63**, 3 (1986).
- [29] J.-P. Bouchaud, M. Cates, J. R. Prakash, and S. F. Edwards, *J. Phys. I* **4**, 1383 (1994).
- [30] A. Aradian, E. Raphaël, and P.-G. de Gennes, *C. R. Phys.* **3**, 187 (2002).
- [31] In the original paper [19] we used power 2.5, however 2.7 gives a better agreement with simulations.
- [32] J. Schäfer, S. Dippel, and D. E. Wolf, *J. Phys. I* **6**, 5 (1996).
- [33] P. A. Cundall and O. D. L. Strack, *Geotechnique* **29**, 47 (1979).
- [34] M. P. Allen and D. J. Tildesley, *Computer Simulations of Liquids* (Oxford University Press, Oxford, 1987).
- [35] T. S. Komatsu, S. Inagaki, N. Nakagawa, and S. Nasuno, *Phys. Rev. Lett.* **86**, 1757 (2001).
- [36] N. Taberlet, P. Richard, A. Valance, W. Losert, J. M. Pasini, J. T. Jenkins, and R. Delannay, *Phys. Rev. Lett.* **91**, 264301 (2003).
- [37] Y. Forterre, *J. Fluid Mech.* **563**, 123 (2006).
- [38] S. B. Savage and K. Hutter, *J. Fluid Mech.* **199**, 177 (1989).
- [39] O. Pouliquen and Y. Forterre, *J. Fluid Mech.* **453**, 133 (2002).